Journal of Metals, Materials and Minerals, 37(1), e2719, 2027

Synergistic multifunctionality in $SrMnO_3$-ZrO_2 composite: Unravelling the dielectric relaxation and enhanced visible-light photocatalytic degradation of ciprofloxacin

Kirttimayee MOHANTA[1], Swayam Aryam BEHERA[1], Aniket PANDA[1], Raj MOHANTY[1], Asima SUBHADARSHINI[2], Binita NANDA[1], and P.Ganga Raju ACHARY[1,*]

[1] *Department of Chemistry, Siksha 'O' Anusandhan (Deemed to be University), Bhubaneswar-751030, India*
[2] *Department of Environmental Science, Siksha 'O' Anusandhan, (Deemed to be University), Bhubaneswar-751030, India*

***Corresponding author e-mail**: pgrachary@soa.ac.in

Received date:
14 April 2026
Revised date:
10 May 2026
Accepted date:
31 May 2026

Keywords:
Dielectric;
Impedance;
Photocatalysis;
Photo-oxidation;
Ciprofloxacin

Abstract

Zirconium modified strontium manganite composite is synthesized using an economically solid-state method. Orthorhombic symmetry is confirmed by structural analysis using X-ray diffraction (XRD) and the SEM analysis reveals the uniform dispersion of elements, chemical composition including morphology. The characteristic stretching and bending modes of the Sr–Mn–O and O–Mn–O bonds in the octahedral SrO_6 unit were identified by Fourier-transform infrared (FTIR) spectroscopy. Optical bandgap values, measured by UV-visible diffuse reflectance spectroscopy (DRS), show a composition-dependent bandgap value of 2.57 eV for the 1:1 ratio. Electrical measurements indicate that the transport mechanism is dominated by a hopping-type charge transfer process. The SMOZr (1:1) composite shows enhanced photocatalytic activity with an efficiency of 88.3% degradation of ciprofloxacin (CIP) under visible light irradiation. The catalyst shows high stability and recyclability over four consecutive cycles. The kinetic studies establish the pseudo-first-order degradation of the pollutant, which highlights the robustness of this stable multifunctional perovskite material for environmental applications.

1. Introduction

The dielectric materials are the basis of various modern technologies, such as energy storage system, actuators, sensors, and high-performance capacitors. Within this scientific realm, perovskite-structured oxides have become the subject of interest because of their very high dielectric constant, almost zero loss of electrical energy, and very flexible electrical properties [1–3]. The viability of perovskite with $SrBO_3$ (B = Ru, Fe, Co, Mn, Ti etc.) formula with divalent Sr ions in the A site as super capacitor electrodes is explored for $SrTiO_3$ [4], $SrRuO_3$ [5], $SrFeO_3$ [6] and $SrMnO_3$ [7] are identified as the promising candidates. Therefore, it is desirable to improve the performance of strontium manganite by modifying its structure and composition. Besides super capacitance, perovskites with $SrBO_3$ (B = Fe, Co, Mn etc.) have been reported as potential for gas sensing [8], oxygen permeation [9], solid state fuel cells [10] and water splitting [11] etc. Recent observation of new phenomena like piezoelectricity, metal-insulator transition [12], and colossal magnetoresistance has sparked a new surge of interest in the research of these materials [13]. Its changes in the structure in normal conditions show a high technological potential, in the form of $SrMnO_3$. This material containing the mid-sized Sr^{2+} ion is an unusual case of a compound with both hexagonal (low-temperature) and cubic (high-temperature) perovskite phases. The magnetic and electronic properties of the materials can be improved by doping[14]. But strontium manganite has some drawbacks such as low fracture toughness, low thermal stability and low band gap.

The most effective method to bypass the intrinsic limitations of the single-phase perovskite is to deliberately incorporate a number of ceramic matrices, such as zirconia, into the $SrMnO_3$. Zirconia is selected mainly because of its high thermal stability, high chemical inertness and high fracture toughness which will give a strong platform to the composite material. The photoactivity of ZrO_2 is also very important, because this is in the structure of the material and can demonstrate photoactivity in both the visible and ultraviolet ranges of light, which allows one to consider it as a material of high potential for use in solar energy and pollutant treatment. The ZrO_2's stable dielectric properties will also be complimented by the high charge transport properties of the manganite, which will enable the $SrMnO_3$-ZrO_2 heterostructures to possess optimized dielectric properties and dielectric loss, as well as enhanced separation of charge carriers for the photocatalytic degradation of recalcitrant pollutants. Recent investigations of analogous $AMnO_3$-ZrO_2 composite systems have demonstrated this principle: Mohanta *et al.* [15] reported that $BaMnO_3$-ZrO_2 composites achieve 89% photocatalytic degradation of Methylene Blue under visible light, attributing the improvement to heterojunction-driven charge separation. Behera *et al.* [16] further demonstrated that manganite-zirconia systems exhibit enhanced dielectric properties relative to the individual components. More broadly, the multifunctional integration of dielectric energy harvesting and photocatalytic remediation in a single perovskite-based platform has been exemplified by Chandrasekaran *et al.* [17] for the $CaCu_3Ti_4O_{12}$ (CCTO) system, which simultaneously enables triboelectric nano generation (74 V output) and

photocatalytic degradation of doxycycline (87% efficiency under visible light). These precedents directly motivate the present work.

The innovative synthesis of $SrMnO_3$-ZrO_2 heterostructures is a tool for studying the interaction of the matrix transition metal perovskite high permittivity ceramic. The above-described composite materials can be used for the production of multifunctional materials, which are superior in terms of the properties of the components. In particular, the high permittivity ceramic matrix of the composite is the material of ZrO_2, which has low loss factors and high permittivity values. On the other hand, the $SrMnO_3$ material has excellent charge transport rate values and high magnetoresistance values. The integrity of the structure and electrical performance is significant particularly in the microelectronic field. Moreover, the unique combination of the components of the composite material can enable the introduction of new light harvesting mechanisms, and therefore, the composite materials can be used in the field of solar chemical catalysis.

The $SrMnO_3$-ZrO_2 heterostructures also exhibit considerable photocatalytic activity, apart from the optimized dielectric properties. The materials should have their photocatalytic activity evaluated for sustaining the environment and the conversion of solar energy to chemical energy. The use of semiconductor photocatalytic materials is a sustainable and efficient way to tackle environmental problems around the world by converting solar energy into chemical energy. The introduction of $SrMnO_3$ into the zirconia structure allows optimization of the electronic structure and band gap of the composite material. The optimized band gap structure allows effective splitting of electron and hole, leading to enhanced catalytic activity of the composite material than the individual materials.

This article will discuss dielectric properties, photocatalytic activities, and its applications and working of strontium manganite zirconia composites. The aim of this article is to provide a comprehensive overview of this promising material, which is expected to have a wide range of applications and a bright future in the field of electronics and environmental technology.

2. Experimental details

The synthesis of $SrMnO_3$ and ZrO_2 precursors, followed by the synthesis of $SrMnO_3$-ZrO_2 heterostructures, was achieved through a multi-step process. These steps are discussed below:

(i) An aqueous solution of strontium nitrate, $Sr(NO_3)_2$, and an aqueous solution of manganese nitrate, $Mn(NO_3)_2$, in a 1:1 molar ratio was mixed. The complexing agent was citric acid, which was heated until reflux was achieved at a predetermined temperature for four hours. Dehydration of the gel was achieved in a laboratory oven at 100°C for several hours, followed by calcination at 650°C for 5 h at a heating rate of $5°C \cdot min^{-1}$ and cooled at $3°C \cdot min^{-1}$ to obtain the pure $SrMnO_3$ powder. (ii) Zirconia (ZrO_2), was synthesized through the controlled precipitation calcination method. Zirconium oxychloride octahydrate, denoted as $ZrOCl_2 \cdot 8H_2O$, was dissolved in ethanol to obtain the precursor solution. A 4 M NaOH solution was added dropwise with constant stirring to precipitate zirconium hydroxide [$Zr(OH)_4$], and the process was continued until precipitation was complete and a uniform dispersion was obtained. To obtain high purity, the precipitate was washed several times with deionized water and ethanol to remove chloride ions and other impurities. The purified $Zr(OH)_4$ was dehydrated at 120°C for several hours, and the dried precursor was calcined in a muffle furnace at 700°C for 2 h to obtain high-purity, fine ZrO_2 powder suitable for composite preparation. (iii) The $SrMnO_3$-ZrO_2 composites were prepared by the conventional solid-state reaction method using the precursors prepared by the above wet chemical methods. Stoichiometric amounts of $SrMnO_3$ and ZrO_2 powders were taken to prepare the target molar compositions of 1:1 (labeled SMOZr 1:1) and 1:2 (labeled SMOZr 1:2). To ensure better interfacial contact and homogeneity of the phases, the individual powders were mechanically ground in an agate mortar and pestle. The ground powders were then packed into alumina crucibles and calcined in a muffle furnace at 950°C for 8 h. After calcination, the samples were furnace-cooled to room temperature, and the sintered materials were ground into a fine powder to enable easy structural and electrical property analysis.

The phase purity and crystal structure of the synthesized composites were analyzed by X-ray diffraction (XRD). For electrical and optical analysis, the powders were pressed into pellets with 1% polyvinyl alcohol (PVA) binder and then subjected to a homogeneous uniaxial pressure of $4 \times 10^6\ Nm^{-2}$ using a potassium bromide (KBr) hydraulic press. The green pellets were then sintered at 1000°C for 8 h to provide structural robustness. To provide a homogeneous surface finish, the sintered samples were polished with fine-grade emery paper. Microstructural analysis and surface morphology were carried out using scanning electron microscopy (SEM). Optical analysis was performed using an Agilent Cary 5000 UV-Vis-NIR spectrometer with a diffuse reflectance system (DRS) in the wavelength range of 300 nm to 600 nm. FTIR spectra were recorded between 1000 cm^{-1} and 4000 cm^{-1} using a PerkinElmer Spectrum instrument to identify functional group vibrations. For electrical measurements, ohmic contacts were established by applying high-grade conductive silver paint (Alfa Aesar) to the opposing parallel faces of the pellets. The dielectric properties, AC conductivity, and complex impedance parameters were then systematically measured using a precision LCR meter.

3. Result and discussion

3.1 XRD

The crystal structure and phase purity of the synthesized materials were also verified using powder XRD, as depicted in Figure 1(a). From the XRD results, it is evident that the synthesized materials form a well-defined dual-phase material, as indicated by the sharp and strong reflections. The first series of reflections, such as those observed at 27.16° (112), 32.74° (020), and 35.10° (203), match perfectly with the orthorhombic structure of $SrMnO_3$ (JCPDS 00-025-0900) with the following parameters: a = 9.4520 Å, b = 5.4670 Å, and c = 9.1050 Å. These reflections are interwoven with the corresponding reflections of cubic ZrO_2 with FM-3M symmetry, as indicated by the strong reflections observed at 30.12° (111) and 34.96° (200), corresponding to the standard value of the lattice parameter a = 5.1280 Å (JCPDS 00-049-1642). The absence of other reflections or shifts in the observed reflections indicates successful incorporation of ZrO_2 into the $SrMnO_3$ matrix without major strain and secondary phases, as verified by the exact match of the observed reflections with those of the standard cards for both materials, indicating the structural integrity of both materials and

providing a solid foundation for further optical and morphological studies [18].

3.2 FTIR

The presence of different percentage of ZrO_2 in $SrMnO_3$ was analyzed by using FTIR as shown in Figure 1(b). The O-H stretching vibration mode occurred between 3650 cm^{-1} and 3300 cm^{-1} [19]. In the higher concentration of Zr, for the carboxylic group, a considerable broad bending at 1440 cm^{-1} was seen. A red shift in the peak ranges from 1400 cm^{-1} to 1300 cm^{-1}. As the Zr component was added into the substance, peak values shifted to the right that is from 2336 cm^{-1} to 2361 cm^{-1} and that was for metal-oxygen. The C-O stretching and bending peaks was observed 1070 cm^{-1} due to presence of primary alcohol. The band at 604 cm^{-1} peak observed due to Zr-O bond. Due to stretching vibration of SrO_6 (octahedral) band observed at 858 cm^{-1}.

3.3 SEM

The surface topography and statistical grain size distribution of the SMOZr (1:1) and SMOZr (1:2) composites are shown in the SEM micrographs (Figure 1(c) and Figure 1(d)). The micrographs clearly reveal the presence of well-defined granular structures, where the grains are evenly distributed across the surface of the material. Although uniform distribution is maintained, the micrographs show varying sizes of the grains, which can be attributed to the complex nucleation mechanisms involved in the solid-state synthesis of the heterostructures. Analysis of the particles reveals that the mean grain size of the SMOZr (1:1) composite is 67.02 nm, with a standard deviation of 28.56. However, an increase in the zirconia content of the SMOZr (1:2) composite results in a decrease in the mean grain size to 52.64 nm, with a standard deviation of 14.62. This variation in morphological properties clearly indicates that the stoichiometric ratio is a decisive factor in controlling the growth kinetics and structural density of the $SrMnO_3$-ZrO_2 heterostructure.

3.4 UV-DRS

The UV-Vis (DRS) analysis of Zr modified $SrMnO_3$ has shown in Figure 2(a). The optical band gap for the samples is calculated by Tauc's equation which is obtained by; $\alpha h\upsilon = A(h\upsilon - E_g)^n$ [20], where α: the absorption co-efficient, υ: light frequency, A: proportionality constant, E_g: band gap, n: transition. For direct transitions, the value of "n" is 1/2, whereas for indirect transitions, it is 2. Figure 2(b). depicts the (αhυ)1/2 vs hυ curve. The band gap value is obtained by making a tangent from the slope to the x-axis. For SMOZr (1:1) and SMOZr (1:2), the obtained band gap values are 2.57 eV and 2.79 eV, respectively. In contrast to SMOZr1:2, the band gap trend is seen to be declining in the case of SMOZr1:1.

3.5 Electrical behavior

A dielectric constant and tangent loss are two fundamental features of dielectric materials. Figure 3(a-b) show the frequency response curves of the dielectric constant (ε_r) and Figure 3(c-d) show the tangent loss (tanδ) at various temperature for SMOZr (1:1) and SMOZr (1:2). Both ε_r and tanδ display an equal trend, meaning that their values decrease as frequency increases. Both ε_r and tanδ are rapidly dropping towards the high frequency zone in the low frequency region. The dipole relaxation process may be the cause of this kind of behavior. Due to characteristics including resistive loss and relaxation loss, dielectric materials have primary shown loss tangent behavior [21].The observed reaction is typical of ferroelectric materials and is in line with the existence of a different sort of polarization mechanism [22]. The polar dielectric characteristics are demonstrated by continuous decrease of the dielectric constant and merge to one at higher frequency. Due to the presence of electronic, ionic, orientation, and space charges, it has been found that certain materials have the greatest dielectric constant, which is 730 at 1 kHz [23].The tanδ variation with frequency exhibits a diminishing tendency when the frequency is raised, and the high temperature calcinated sample keeps the lowering trend of these losses, demonstrating the accuracy of the XRD patterns. Lower estimates of these losses are typically associated with the development of quick electrical gadgets.

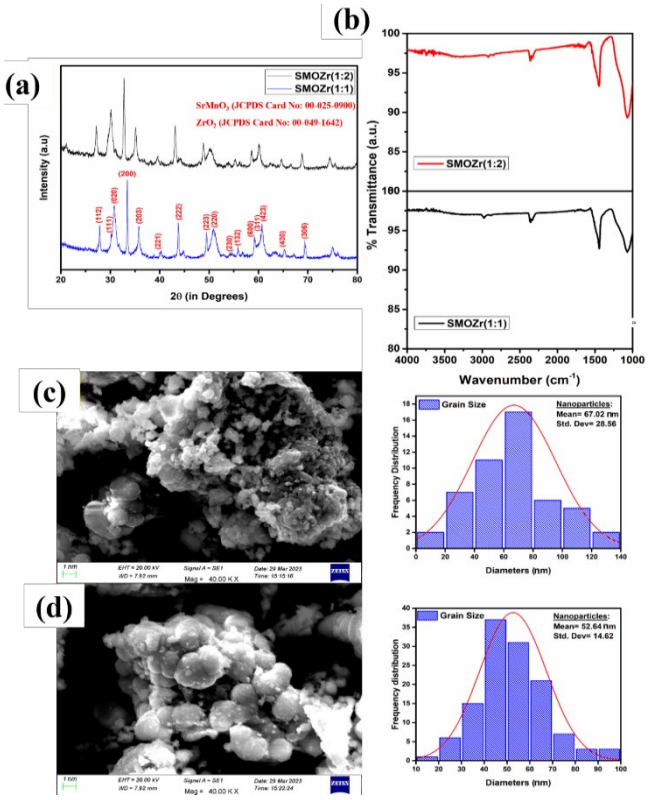

Figure 1. (a) XRD pattern, (b) FTIR spectra, (c) and (d) SEM images with grain size of $SrMnO_3$:ZrO_2 (1:1) and $SrMnO_3$:ZrO_2 (1:2) respectively.

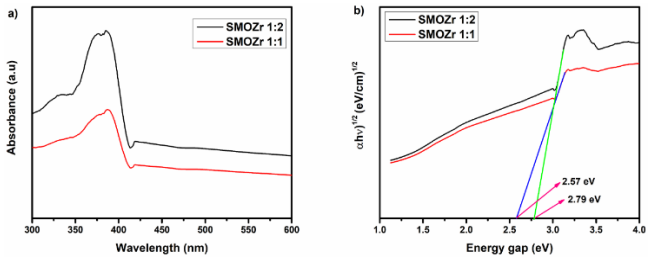

Figure 2. (a) UV-DRS plot, (b) Band-gap analysis by Taus's Plot of $SrMnO_3$:ZrO_2 (1:1) and $SrMnO_3$:ZrO_2 (1:2).

Wagner and Maxwell's model [22] can be used to show the decreasing trend of ε_r and tanδ towards the high-frequency zone. The conventional dielectric medium has less conducting grain borders and highly conducting grains, according to this concept. The hopping of electrons between Mn ions at the octahedral site may be cause of the decline in Er towards higher frequency. The collection of electrons is taking place nearby creating space-charge polarization as a result of high resistive behaviors at grain boundaries. As a result, the dielectric permittivity is greater close to the low frequency region and gradually decrease as the frequency increases. In case of SMOZr (1:1) and SMOZr (1:2), it has been seen that ε_r value decrease gradually with increase in frequency (Hz) but in case of tanδ vs Frequency graph of above two sample, seen that tanδ value increase with rise in temperature at low frequency range, then decreases with high frequency range.

Figure 3(e-f) shows the frequency dependent AC-Conductivity (σ_{AC}) for SMOZr (1:1) and SMOZr (1:2). The value of σ_{AC} was calculated by using the expression: $\sigma_{AC} = \omega\varepsilon_r\varepsilon_0 \tan\delta$. Each term (variable) has their usual meanings. The graph shows that the value of AC conductivity increases in the higher frequency region for both prepared sample SMOZr (1:1) and SMOZr (1:2). The increased ac conductivity in higher frequency of Samples increase the activation energy of the samples.

Figure 4(a-b) show the variation of the real impedance Z' for SMOZr (1:1&1:2), and Figure 4(c-d) show the variation of the imaginary impedance Z'' for SMOZr (1:1&1:2). The pattern is evident: as the frequency increases, Z' decreases steadily, and after 10^4 Hz, the curves merge. This indicates that beyond 10^4 Hz, the effect of space-charge discharge reduces the barrier and hence the impedance [16,24]. The Z' value decreases with an increase in temperature, which is reminiscent of a semiconductor-like NTCR (negative temperature coefficient of resistance) property. At high frequencies, the Z'' value approaches a constant value for all temperatures. This trend suggests that the SMOZr (1:1) and SMOZr (1:2) compounds possess a frequency-dependent property. The full width at half maximum of the Z'' peak is a measure of relaxation-time dispersion.

The progressive decrease in peak height indicates the involvement of a relaxation process. The relaxation peak shifts to higher frequencies with increasing temperature. From the complex impedance diagrams, the bulk resistance of the sample can be determined. This is expressed as $\sigma = t / (R_g A)$, where σ is the AC conductivity, R_g is the bulk resistance, A is the cross-sectional area, and t is the thickness of the sample. The imaginary part of impedance, denoted by Z'', was used to obtain the fitting parameters based on the Nyquist plots. In this context, different electrical parameters, e.g., bulk capacitance, denoted by C_b; constant phase element, denoted by Q; bulk resistance, denoted by R_b; grain boundary capacitance, denoted by C_{gb}; grain boundary resistance, denoted by R_{gb}; and frequency exponent, denoted by n, were extracted over a wide range of temperature, ranging from 25°C to 500°C. The impedance data were employed to fit the data by employing a CQR–CR equivalent circuit model which are shown in Figure 4(e-f) The calculated parameters for the SMOZr (1:1) and SMOZr (1:2) samples are listed in Table 1-2 respectively.

3.6 Photocatalytic degradation experiment

The photocatalytic activities of the SMOZr (1:1) and SMOZr (1:2) composites under visible light irradiation were examined, and ciprofloxacin was used as a model pollutant. For the experiment, a solution of 20 mL, 60 ppm ciprofloxacin, was prepared. Then, 0.02 g

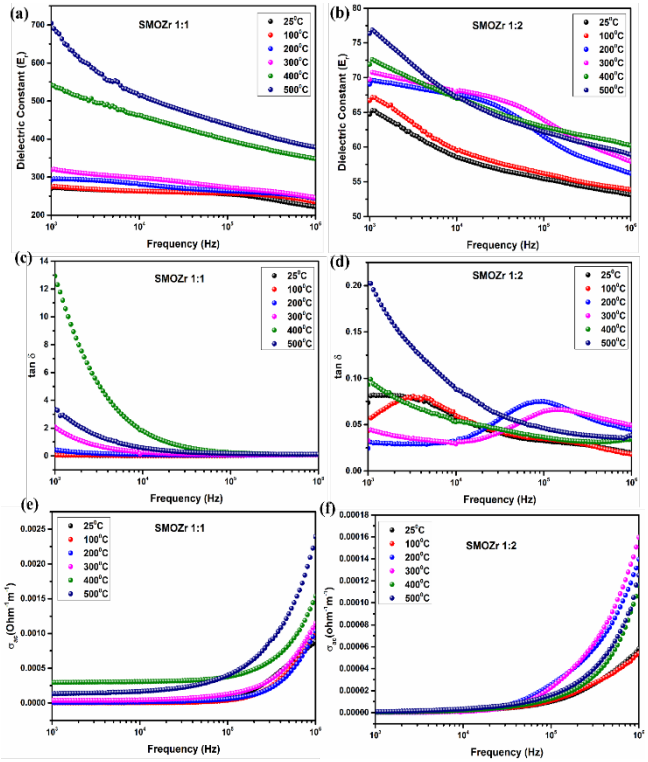

Figure 3. (a) and (b) Dielectric Constant (ε_r) vs frequency, (c) and (d) tanδ vs frequency, (e) and (f) σ_{AC} vs frequency of $SrMnO_3$:ZrO_2 (1:1) and $SrMnO_3$:ZrO_2 (1:2).

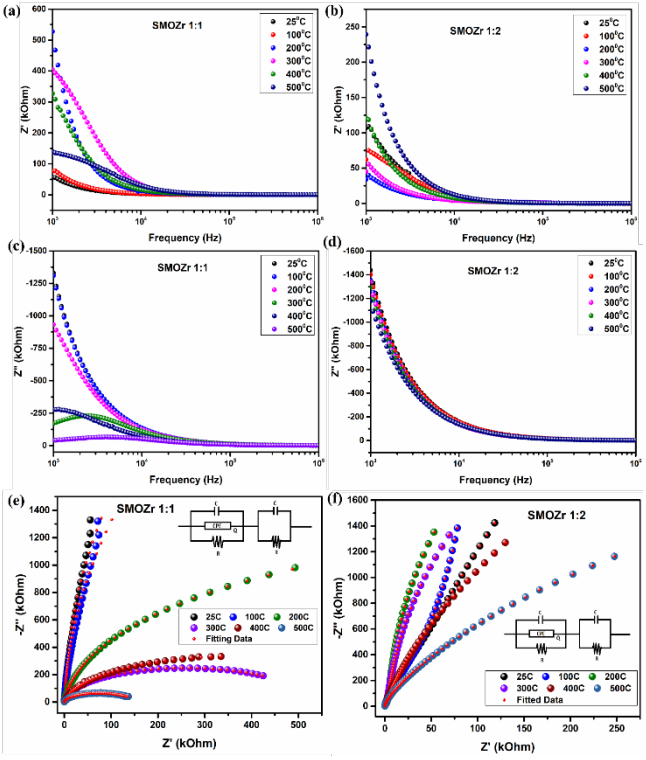

Figure 4. (a) and (b) Real impedance (Z') vs frequency, (c) and (d) Imaginary impedance (Z'') vs frequency, (e) and (f) Nyquist plot of $SrMnO_3$:ZrO_2 (1:1) and $SrMnO_3$:ZrO_2 (1:2).

of the photocatalyst was added to the solution. Before the photocatalytic reaction, the solution was stirred in the dark for 15 min to attain adsorption-desorption equilibrium between the photocatalyst and the pollutant molecules, Once the equilibrium was attained, the solution was exposed to sunlight for 90 min to execute the photocatalytic reaction. After the photocatalytic reaction, the photocatalyst was filtered out, and the solution was recorded using a UV-Vis spectrophotometer (Systronics-2022) at a wavelength of 273 nm, since the solution was clear. Then, the photocatalytic degradation of ciprofloxacin was determined using the following equation and the picture depicting before and after degradation of ciprofloxacin is shown in Figure 5.

$$\text{Degradation efficiency (\%)} = \frac{C_0 - C_t}{C_t} \times 100$$

Where, C_0 is the initial CIP concentration ($mg \cdot L^{-1}$) and C_t is the residual concentration at irradiation time t (min).

3.6.1 Photo-oxidation of ciprofloxacin:

Photo-oxidation of ciprofloxacin was done using two prepared semiconducting-photocatalysts SMOZr (1:1) and SMOZr (1:2) and compared. Different parameters are responsible for photocatalytic oxidation process. **(i) Adsorption-desorption study**: The adsorption-desorption equilibrium analysis was carried out to determine the optimal time for the photooxidation process is shown in Figure 6(a). The reaction was first carried out by taking SMOZr 1:1 as the reference catalyst in the dark for 15 min, then was carried under visible light for 90 min with 15 min time interval. The absorbance peak was recorded to be appeared at 273 nm and the intensity of the peak gradually decreases as time increases from 15 min to 90 min which concluded that at 90 min the absorption of ciprofloxacin is higher. The absorption capacity (A/A_0) is directly correlated with the absorption concentration (C/C_0) and the optimum time set for further photooxidation of ciprofloxacin is 90 mins. The photo degradation is directly proportional to the amount of substrate adsorbed on the surface of the catalyst. **(ii) Effect of pH:** The surface chemistry of the catalyst varies with pH, which has a substantial impact on photocatalytic activity. Figure 6(b) shows the effect of pH on the degradation of ciprofloxacin under light. Prior to the photocatalytic degradation process, ciprofloxacin is expected to adsorb on the SMOZr catalyst even in the absence of light due to the interaction of opposite charges. pH is very important in this study since the chemical structure of ciprofloxacin is pH-dependent. In particular, below pH 5.5, ciprofloxacin is a cationic compound because of the deprotonation of the $–NH_2$ group [25]. Above pH 7.7, it becomes anionic, while between pH 5.5 and 7.5, it is a zwitterion [26]. The photocatalyst surface, like most materials, has pH-dependent charges, which are positive on some surfaces and negative on others. For SMOZr, in a 1:1 ratio, the pHpzc is 7.6. This implies that if the pH of the surrounding environment is higher than 7.6, the surface will be negatively charged due to the attraction of hydroxide ions. Notably, the adsorption capacity decreases in alkaline environments because of the electrostatic repulsion between the negatively charged surface and ciprofloxacin.

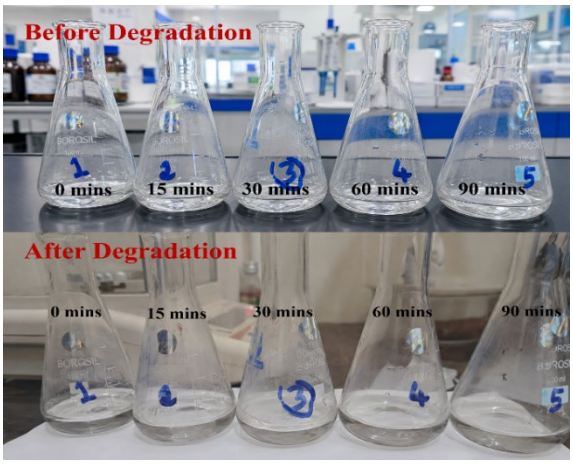

Figure 5. Photographs of photodegradation experiment of CIP in various time intervals before and after degradation.

Table-1. Significance of Grain and grain boundary resistance and capacitance: at selected temperatures for SMOZr (1:1).

Temp. [°C]	C_b [$nFcm^{-2}$]	Q [$S\text{-}sec^5cm^{-2}$]	R_b [kΩ]	C_{gb}]$nFcm^{-2}$]	R_{gb} [kΩ]	Frequency power [n]
25	3.40×10^{-10}	1.02×10^{-5}	1.85×10^{12}	1.18×10^{-10}	2.42×10^{7}	3.33×10^{-1}
100	7.79×10^{-21}	2.95×10^{-7}	3.26×10^{4}	1.20×10^{-10}	1.90×10^{7}	6.19×10^{-1}
200	6.11×10^{-23}	8.40×10^{-9}	3.25×10^{4}	1.35×10^{-10}	2.46×10^{6}	8.26×10^{-1}
300	6.67×10^{-17}	1.94×10^{-9}	1.49×10^{5}	1.80×10^{-10}	3.77×10^{5}	8.76×10^{-1}
400	5.98×10^{-11}	4.07×10^{-10}	7.50×10^{5}	6.55×10^{-19}	1.45×10^{1}	9.06×10^{-1}
500	2.01×10^{-24}	5.12×10^{-10}	1.34×10^{5}	7.66×10^{-9}	2.16×10^{4}	9.30×10^{-1}

Table-2. Significance of Grain and grain boundary resistance and capacitance: at selected temperatures for SMOZr (1:2).

Temp. [°C]	C_b [$nFcm^{-2}$]	Q [$S\text{-}sec^5cm^{-2}$]	R_b [kΩ]	C_{gb}]$nFcm^{-2}$]	R_{gb} [kΩ]	Frequency power [n]
25	2.90×10^{-10}	4.12×10^{-9}	9.16×10^{4}	1.14×10^{-10}	3.80×10^{7}	7.89×10^{-1}
100	2.87×10^{-10}	3.87×10^{-9}	9.50×10^{4}	1.18×10^{-10}	2.53×10^{8}	7.84×10^{-1}
200	4.04×10^{-10}	2.30×10^{-7}	7.00×10^{3}	1.18×10^{-10}	3.91×10^{7}	5.19×10^{-1}
300	4.16×10^{-10}	2.09×10^{-6}	1.30×10^{17}	1.20×10^{-10}	3.02×10^{7}	3.97×10^{-1}
400	9.09×10^{-11}	1.31×10^{-10}	3.54×10^{7}	6.16×10^{2}	9.95×10^{5}	8.46×10^{-1}
500	8.82×10^{-11}	1.48×10^{-10}	9.54×10^{6}	2.03×10^{-9}	1.83×10^{4}	8.64×10^{-1}

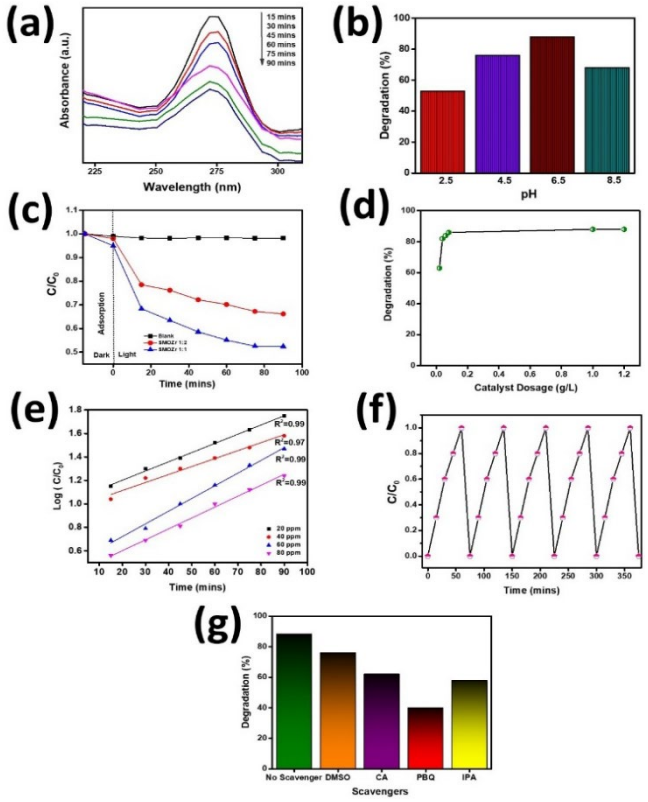

Figure 6. (a) absorbance spectra of ciprofloxacin over SMOZr 1:1 composite with respect to time, (b) Effect of pH, (c) rate of ciprofloxacin degradation over photocatalysts with time interval, (d) Effect of catalyst dose, (e) kinetic plot of ciprofloxacin degradation over different concentration, (f) Reusability, (g) Effect of active radical reagents.

The photocatalytic degradation of ciprofloxacin is at its highest when the ciprofloxacin solution is at a pH of 6.5, which is the default pH for this solution. These results clearly indicate that optimal ciprofloxacin adsorption is essential for optimal photocatalytic degradation. This can be attributed to surface phenomenon-driven photocatalysis or adsorptive photocatalysis. Therefore, all subsequent experiments involving ciprofloxacin degradation were carried out at a pH of 6.5.

(**iii) Degradation efficiency**: The rate of degradation of ciprofloxacin is compared between the two catalysts SMOZr 1:1 and SMOZr 1:2 is depicted in Figure 6(c). which shows that catalyst SMOZr 1:1 has the highest efficiency of degradation ciprofloxacin in 90 min as compared to SMOZr 1:2. **(iv) Effect of catalyst dose**: The effect of catalyst concentration on ciprofloxacin solution was studied on the the catalyst SMOZr 1:1. when demonstrated in Figure 6(d). Because there were more active sites and free radicals as the catalyst concentration raised from 0.02 $g{\cdot}L^{-1}$ to 1.2 $g{\cdot}L^{-1}$, the photo-degradation efficiency improved as well. The clearance efficiency either remains constant or declines above 1 $g{\cdot}L^{-1}$. This might be the effect of the solution's higher concentration of catalyst blocking light penetration and lowering efficiency. As a result, 1 $g{\cdot}L^{-1}$ can be deemed the best catalyst concentration for all trials, with an 88.30% degradation rate. **(v) Effect of kinetics:** The kinetics study was evaluated by taking different concentrations of ciprofloxacin ((20 $mg{\cdot}L^{-1}$, 40 $mg{\cdot}L^{-1}$, 60 $mg{\cdot}L^{-1}$, and 80 $mg{\cdot}L^{-1}$) at different irradiation (15 min, 30 min, 45 min, 60 min, 75 min, and 90 min) time shown in Figure 6(e). In order to study photocatalytic degradation, a pseudo first order model was fitted to the data using the formula $\log C/(C_0) = Kt$, where K is the actual reaction constant, C is the residual concentration following illumination time t, and C_0 is the solution's initial concentration. Table 3 displays a comparison between the ciprofloxacin regression coefficient and K. **(vi) Reusability and stability test:** Reusing used photocatalysts has commercial advantages in a variety of industrial uses. Hence, Figure 6(f). depicts the results of the reusability investigation that was done on the employed photocatalyst. After five successive cycles, our optimized sample SMOZr 1:1 demonstrates exceptional reusability; also, the photocatalytic degradation efficiency has not been significantly reduced, indicating that no Sr, Mn, or Zr ions are leached into the solution. **(vii) Reactive species study:** The photooxidation of SMO/Zr 1:1 requires investigation of the surface photogenerated carriers as well as active materials that predominate the photooxidation of pollutants. Various scavenging agents, such as isopropanol, para-benzoquinone, dimethyl sulphoxide and citric acid, are used to trap the potential active radicals OH^-, O_2^-, e^- and h^+, respectively, at a concentration of 1 mM. Figure 6(g)**.** illustrates the impact of several scavenging agents upon the photocatalytic degradation process. From the figure it was observed that ciprofloxacin degradation was supressed during the addition of parabenzoquinone and isopropanol. At the same time, by the use of dimethyl sulphoxide, the degradation efficiency is higher than other scavenging agents. Thus, it may be said that super oxide and hydroxyl radicals are the main active oxidative radicals for ciprofloxacin. Table 4 outlines previous research using a range of photocatalysts in contrast to the current investigation.

Table 3. The kinetic data acquired from the prepared sample of ciprofloxacin degradation.

Concentration of ciprofloxacin	K- app(min^{-1})	Regression Coefficient (R^2)
20 ppm	0.0138	0.99
40 ppm	0.0157	0.97
60 ppm	0.017	0.99
80 ppm	0.019	0.99

Table 4. In comparison to this study, recent work employing different photocatalysts.

Sl. No.	Catalyst	Degrading element	Time	Degradation percentage	References
1.	AgZrP	Methylene Blue	70 mins	90%	[27]
2.	Zr/TiO_2	Chloridazon, Phenol,4-Chlorophenol	4hrs, 30mins	99%, 16%,30%	[28]
3.	**SMOZr**	**Ciprofloxacin**	**90mins**	**88.30 %**	**In this Study**

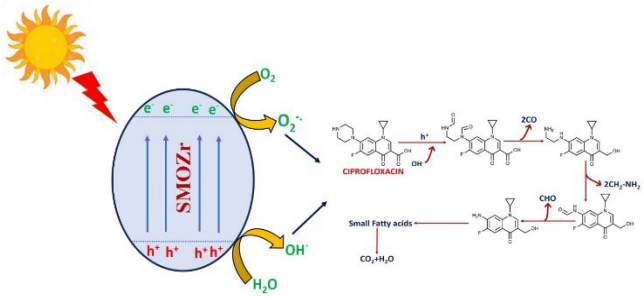

Scheme 1. Schematic Diagram of the Photocatalytic Degradation of Ciprofloxacin over SMOZr1:1

3.6.2 Photocatalytic mechanistic pathway

The mechanistic pathway of degradation/mineralization of ciprofloxacin by the use of the prepared photocatalyst SrMnZr (1:1) was shown in Scheme 1. During the exposure of sunlight on the surface of photocatalyst, photo-generated charge carriers (e^- and h^+) are developed. The electrons in the valence band jumped to the conduction band and holes are created in valence band. The addition of ZrO_2 with $SrMnO_3$ encourages the transfer of electron and reduces the electron-hole recombination. The holes are reacted to the surface adsorbed water to form hydroxyl ($^{\bullet}OH$) radicals and at the same time e^-s are reacted to the atmospheric oxygen to form super oxide ($^{\bullet}O_2^-$) radicals. During the reaction process different intermediate radicals are formed and also influence the rate of degradation of ciprofloxacin and the steps involved in the reaction process is as follows:

$$SMOZr + h\upsilon\ (\lambda > 400\ nm) \rightarrow SMOZr\ (e^-_{cb}) + SMOZr\ (h^+_{vb})$$

$$SMOZr\ (h^+_{vb}) + H_2O \rightarrow H^+ + {}^{\bullet}OH$$

$$SMOZr\ (h^+_{vb}) + OH^- \rightarrow {}^{\bullet}OH$$

$$SMOZr\ (e^-_{cb}) + O_2 \rightarrow {}^{\bullet}O_2^-$$

$$SMOZr\ (e^-_{cb}) + {}^{\bullet}O_2^- + 2H^+ \rightarrow H_2O_2$$

$$2{}^{\bullet}O_2^- + 2H^+ \rightarrow O_2 + H_2O_2$$

$${}^{\bullet}O_2^- + 2H^+ \rightarrow H{}^{\bullet}O_2$$

$$2H^+ + 2H{}^{\bullet}O_2 \rightarrow O_2 + H_2O_2$$

$$H_2O + {}^{\bullet}O_2^- \rightarrow OH^- + {}^{\bullet}OH$$

$$H_2O_2 + {}^{\bullet}O_2^- \rightarrow OH^- + {}^{\bullet}OH + O_2$$

$$\text{Ciprofloxacin} + ({}^{\bullet}OH\ /\ {}^{\bullet}O_2^-\ /\ H{}^{\bullet}O_2{}^{\cdot}) \rightarrow \text{Mineralization products}\ (CO_2 + H_2O)$$

4. Conclusion

Zirconium-modified strontium manganite (SMOZr) was successfully synthesized via a cost-effective high-temperature solid-state route. Structural, morphological, and spectroscopic analyses confirmed the formation of an orthorhombic perovskite phase with uniformly distributed grains and characteristic vibrational modes. Optical studies revealed a suitable band gap, while dielectric and ferroelectric investigations demonstrated promising functional properties. Conductivity analysis indicated that charge transport occurs predominantly through a hopping mechanism. Among the synthesized compositions, SMOZr (1:1) exhibited superior photocatalytic performance, achieving 88.3% degradation of ciprofloxacin and maintaining excellent stability over four successive cycles. The pseudo-first-order kinetic behavior further confirmed its effective catalytic activity. These results highlight the potential of SMOZr as a stable, economical, and environmentally friendly material for advanced photocatalytic wastewater treatment applications.

Reference

[1] S. K. Abbas, S. Atiq, S. Riaz, S. M. Ramay, and S. Naseem, "Thermally assisted electro-active regions in $SrMnO_3$ ceramics," *Materials Chemistry and Physics*, vol. 200, pp. 128–135, 2017.

[2] S. J. Heo, M. Sanders, R. O'Hayre, and A. Zakutayev, "Double-site substitution of Ce into (Ba, Sr) MnO_3 perovskites for solar thermochemical hydrogen production," *ACS Energy Letters*, vol. 6, no. 9, pp. 3037–3043, 2021.

[3] P. G. R. Achary, A. A. Nayak, R. K. Bhuyan, R. N. P. Choudhary, and S. K. Parida, "Effect of cerium dopant on the structural and electrical properties of $SrMnO_3$ single perovskite," *Journal of Molecular Structure*, vol. 1226, p. 129391, 2021.

[4] K. Karthick, S. R. Ede, U. Nithiyanantham, and S. Kundu, "Low-temperature synthesis of $SrTiO_3$ nanoassemblies on DNA scaffolds and their applications in dye-sensitized solar cells and supercapacitors," *New Journal of Chemistry*, vol. 41, no. 9, pp. 3473–3486, 2017.

[5] P. M. Wilde, T. J. Guther, R. Oesten, and J. Garche, "Strontium ruthenate perovskite as the active material for supercapacitors," *Journal of Electroanalytical Chemistry*, vol. 461, no. 1–2, pp. 154–160, 1999.

[6] F. Deganello, L. F. Liotta, S. G. Leonardi, and G. Neri, "Electrochemical properties of Ce-doped $SrFeO_3$ perovskites-modified electrodes towards hydrogen peroxide oxidation," *Electrochimica Acta*, vol. 190, pp. 939–947, 2016.

[7] S. Demirel, E. Oz, S. Altin, A. Bayri, O. Baglayan, E. Altin, and S. Avci, "Structural, magnetic, electrical and electrochemical properties of $SrCoO_{2.5}$, $Sr_9Co_2Mn_5O_{21}$ and $SrMnO_3$ compounds," *Ceramics International*, vol. 43, no. 17, pp. 14818–14826, 2017.

[8] Y. Wang, J. Chen, and X. Wu, "Preparation and gas-sensing properties of perovskite-type $SrFeO_3$ oxide," *Materials Letters*, vol. 49, no. 6, pp. 361–364, 2001.

[9] X. Chen, L. Huang, Y. Wei, and H. Wang, "Tantalum stabilized $SrCoO_3$-δ perovskite membrane for oxygen separation," *Journal of Membrane Science*, vol. 368, no. 1–2, pp. 159–164, 2011.

[10] A. Aguadero, D. Pérez-Coll, J. A. Alonso, S. J. Skinner, and J. Kilner, "A new family of Mo-doped SrCoO3-δ perovskites for application in reversible solid state electrochemical cells," *Chemistry of Materials*, vol. 24, no. 14, pp. 2655–2663, 2012.

[11] S. Gholamrezaei, and M. Salavati-Niasari, "Sonochemical synthesis of $SrMnO_3$ nanoparticles as an efficient and new catalyst for O_2 evolution from water splitting reaction," *Ultrasonics Sonochemistry*, vol. 40, pp. 651–663, 2018.

[12] A. K. Raychaudhuri, "Metal-insulator transition in perovskite oxides: a low-temperature perspective," *Advances in Physics*, vol. 44, no. 1, pp. 21–46, 1995.

[13] A. P. Ramirez, "Colossal magnetoresistance," *Journal of Physics: Condensed Matter*, vol. 9, no. 39, p. 8171, 1997.

[14] G. Pan, X. Bai, D. Yang, X. Chen, P. Jing, S. Qu, L. Zhang, W. Xu, B. Dong, and H. Song, "Doping lanthanide into perovskite nanocrystals: highly improved and expanded optical properties," *Nano letters*, vol. 17, no. 12, pp. 8005–8011, 2017.

[15] K. Mohanta, S. A. Behera, B. Nanda, and P. G. R. Achary, "Facile synthesis of $BaMnO_3$-ZrO_2 composite: A step towards the photo-catalytic degradation of organic dye," *Journal of Metals, Materials and Minerals*, vol. 35, no. 3, p. e2233, 2025.

[16] S. A. Behera, S. Panda, S. Hajra, B. K. Panigrahi, H. J. Kim, and P. G. R. Achary, "EVA/PZT composite-based triboelectric nanogenerator for energy harvesting," *Energy Technology*.

[17] K. R. Kaja, S. A. Behera, B. Das, S. Hajra, S. Panda, M. A. Belal, N. Vittayakorn, B. Nanda, P. G. R. Achary, and H. J. Kim, "Calcium copper titanate particles based energy harvesting and removal of pharmaceutical pollutants," *ACS Applied Electronic Materials*, vol. 7, no. 9, pp. 4327–4338, 2025.

[18] A. Kumari, K. Kumari, F. Ahmed, A. Alshoaibi, P. A. Alvi, S. Dalela, M. M. Ahmad, R. N. Aljawfi, P. Dua, A. Vij, And S. Kumar, "Influence of Sm doping on structural, ferroelectric, electrical, optical and magnetic properties of $BaTiO_3$," *Vacuum*, vol. 184, p. 109872, 2021.

[19] J. Ingrin, J. Liu, C. Depecker, S. C. Kohn, E. Balan, and K. J. Grant, "Low-temperature evolution of OH bands in synthetic forsterite, implication for the nature of H defects at high pressure," *Physics and Chemistry of Minerals*, vol. 40, pp. 499–510, 2013.

[20] P. Makuła, M. Pacia, and W. Macyk, "How to correctly determine the band gap energy of modified semiconductor photocatalysts based on UV-Vis spectra," *Journal of physical chemistry letters*, vol. 9, no. 23, pp. 6814–6817, 2018.

[21] S. Sil, J. Datta, M. Das, R. Jana, S. Halder, A. Biswas, D. Sanyal, and P. P. Ray, "Bias dependent conduction and relaxation mechanism study of Cu_5FeS_4 film and its significance in signal transport network," *Journal of Materials Science: Materials in Electronics*, vol. 29, no. 6, pp. 5014–5024, 2018.

[22] K. Parida, S. K. Dehury, and R. N. P. Choudhary, "Structural, electrical and magneto-electric characteristics of complex multi-ferroic perovskite $Bi_{0.5}Pb_{0.5}Fe_{0.5}Ce_{0.5}O_3$," *Journal of Materials Science: Materials in Electronics*, vol. 27, pp. 11211–11219, 2016.

[23] R. Das, and R. N. P. Choudhary, "Studies of electrical, magnetic and leakage-current characteristics of double perovskite: Dy_2CoMnO_6," *Journal of Alloys and Compounds*, vol. 853, p. 157240, 2021.

[24] S. A. Behera, R. N. P. Choudhary, and P. G. R. Achary, "Electrical and dielectric properties of EVA/modified lead titanate elastomer composites," *Materials Today: Proceedings*, 2023.

[25] S. A. Behera, A. Amanat, and P. G. R. Achary, "Photocatalytic degradation of ciprofloxacin drug utilizing novel PVDF/polyaniline/lanthanum strontium manganate@ Ag composites," *Journal of Metals, Materials and Minerals*, vol. 34, no. 1, p. 1896, 2024.

[26] A. K. Al-Buriahi, M. M. Al-shaibani, R. M. S. R. Mohamed, A. A. Al-Gheethi, A. Sharma, and N. Ismail, "Ciprofloxacin removal from non-clinical environment: A critical review of current methods and future trend prospects," *Journal of Water Process Engineering*, vol. 47, p. 102725, 2022.

[27] Z. Barhon, N. Saffaj, A. Albizane, M. Azzi, R. Mamouni, and M. El Haddad, "Effect of modification of zirconium phosphate by silver on photodegradation of methylene blue," *Journal of Materials and Environmental Sciences*, vol. 3, no. 5, pp. 879–884, 2013.

[28] A. Mbiri, D. H. Taffa, E. Gatebe, and M. Wark, "Zirconium doped mesoporous TiO_2 multilayer thin films: Influence of the zirconium content on the photodegradation of organic pollutants," *Catalysis Today*, vol. 328, pp. 71–78, 2019.